Size-resolved chemical composition, effective density, and optical properties of biomass burning particles

Jinghao Zhai[1], Xiaohui Lu[1], Ling Li[1], Qi Zhang[1,2], Ci Zhang[1], Hong Chen[1], Xin Yang[1]*, Jianmin Chen[1]

[1]*Shanghai Key Laboratory of Atmospheric Particle Pollution and Prevention, Department of Environmental Science and Engineering, Fudan University, Shanghai 200433, China*

[2]*Department of Environmental Toxicology, University of California, Davis, California 95616, United States*

Correspondence to: Xin Yang (yangxin@fudan.edu.cn)

Abstract. Biomass burning aerosol has important impact on the global radiative budget. A better understanding of the correlations between the mixing states of biomass burning particles and their optical properties is the goal of a number of current studies. In this work, effective density, chemical composition, and optical properties of rice straw burning particles in the size range of 50-400 nm were measured using a suite of online methods. We found that the major components of rice straw burning particles included black carbon (BC), organic carbon (OC) and potassium salts, but the mixing states of particles were strongly size-dependent. Particles of 50 nm had the smallest effective density (1.16 g/cm^3), due to a relatively large proportion of aggregate BC. The average effective densities of 100-400 nm particles ranged from 1.35-1.51 g/cm^3 with OC and inorganic salts as dominant components. Both density distribution and single-particle mass spectrometry showed more complex mixing states in larger particles. Upon heating, the separation of the effective density distribution modes testified the external mixing state of less volatile BC or soot and potassium salts. Size-resolved optical properties of biomass burning particles were investigated at two wavelengths (λ=450 & 530 nm). The single scattering albedo (SSA) showed the lowest value for 50 nm particles (0.741±0.007 & 0.889±0.006) because of the larger proportion of BC content. Brown carbon played an important role for the SSA of 100-400 nm particles. The Ångström absorption exponent (AAE) values for all particles were above 1.6, indicating the significant presence of brown carbon in all sizes. Though freshly emitted, the light absorption enhancement (E_{abs}) was observed for particles larger than 200 nm because of the non-BC material coating. Concurrent measurements in our work provide a basis for discussing the physicochemical properties of biomass burning aerosol and its effects on global climate and atmospheric environment.

1 Introduction

Biomass burning is a significant source of trace gases and aerosol particles (Andreae and Merlet, 2001). Biomass burning particles affect climate by both absorbing and scattering solar radiation (Chand et al., 2009) and serve as cloud condensation nuclei which would modify cloud microphysical properties (Petters et al., 2009). In addition, biomass burning particles have considerable impacts on air quality, regional visibility,

and human health (Naeher et al., 2007; Park et al., 2006). Global annual emissions of black carbon (BC) and organic carbon (OC) aerosols are estimated to be ~8 and 33.9 Tg yr^{-1} while open burning contributes approximately 42% for BC and 74% for OC (Bond et al., 2004). Along with rapid economic development and increase in agricultural activities, emissions from agricultural residue combustion in China have drawn extensive attention. The total amount of straws from open burning in China is estimated to be ~140 Tg yr^{-1} (Cao et al., 2008).

Mixing state, composition, and morphology of particles can influence their radiative properties. BC, which is predominantly produced from the combustion related sources, absorbs solar radiation across the visible spectrum, resulting in a warming effect (Bond et al., 2013). An enhancement of BC forcing by up to a factor of 2.9 is estimated by models when BC is internally mixed with other components compared with externally mixed scenarios (Jacobson 2001). The co-emission of BC and OC can lead to internally mixed particles, in which the OC coating can enhance particle absorption through lensing effects (Bond and Bergtrom, 2006; Schnaiter et al., 2005). For internally mixed BC, the assumption of a void-free BC sphere with a material density of 1.8 g/cm^3 can lead to overestimations of the shell/core ratio and absorption enhancement by ~13 and ~17%, respectively (Zhang et al., 2016). In addition to absorption enhancement by internal mixing, some organic matter containing specific functional groups (e.g. nitrated/polycyclic aromatics, phenols) can itself absorb radiation in the short wavelength visible and UV wavelengths (Hoffer et al., 2006; Jacobson, 1999) and is referred to as brown carbon (BrC). As biomass burning is a significant source of BrC, the optical properties of biomass burning particles need to be further understood. Field works have been conducted to measure the light absorption enhancement by particle coatings in different areas (Chan et al., 2011; Nakayama et al., 2014). The degree to which particles absorb light depends on their composition, shape, and mixing state. Researches on chemical composition and mixing state of biomass burning particles have been done by our group members previously (Huo et al., 2016; Zhai et al., 2015). However, it remains unclear how mixing states and chemical composition of biomass burning particles influence their morphology and optical properties.

Particles emitted from biomass burning are generally composed of a mixture of spherical and non-spherical particles and chain aggregates (Martins et al., 1998). Scanning electron microscopy (SEM) as well as transmission electron microscopy (TEM) are common techniques widely used to investigate the morphology of biomass burning particles (China et al., 2013; Giordano et al., 2015; Hopkins et al., 2007). However, these methods are unable to provide continuous "on-line" information and suffer from limitations arising from primary particle overlap, screening effects, and cluster anisotropy (Wentzel et al., 2003). Effective density is a good predictor for the complex properties of biomass burning particles (Pitz et al., 2008) and is often used to convert particle size distributions into mass loading (Schmid et al., 2007). Variations in particle effective density can be used to follow compositional transformations during chemical reactions (Katrib et al., 2005). Online measurements which provide real-time monitoring of particle effective density variation have been developed.

Kelly and McMurry (1992) developed a density measurement technique based on the selection of a monodisperse aerosol with a Differential Mobility Analyzer (DMA) followed by classification according to aerodynamic diameter with an impactor. McMurry et al. (2002) reported a technique to determine size-resolved effective density based on using an Aerosol Particle Mass analyzer (APM) to measure the mass of particles that had been classified according to electrical mobility by a DMA. The DMA-APM method has been applied extensively in field studies as well as laboratory experiments (Hu et al., 2012; Barone et al., 2011). However, few measurements of the effective density of biomass burning particles have been done due to the lack of accompanying on-line chemical information.

Mixing state of individual particle can be very different caused by the chemical composition, aging degree, etc., which greatly influence the morphology and optical property of particles. Thus, distinctions among particles might be omitted by bulk measurements. Single particle mass spectrometry techniques have been utilized to measure the chemical composition, size, density, and shape of individual particles. Spencer et al. (2007) utilized a DMA-ultrafine aerosol time-of-flight mass spectrometer (UF-ATOFMS) system to detect the effective density and chemical composition simultaneously of ambient aerosol at single-particle level. The comprehensive information about single particles could help to elucidate the morphology, mixing state, and sphericity of biomass burning particles.

The chemical composition, morphology, and optical properties of particles are usually interrelated. Biomass burning particle is a complex mixture of organic and inorganic species, including strongly light-absorbing BC and BrC. Size-resolved or even single particle level information on the morphology, chemical composition, and optical properties of biomass burning particles are necessary to have a better understanding of the correlations among these physiochemical properties. In this study, laboratory experiments were conducted on rice straw combustion, a main source of biomass burning particles in Southern China. The size-resolved effective density of biomass burning particles was measured by two different methods. One was based on a DMA-APM-Condensation Particle Counter (CPC) system. For the other method, the mobility size-selected particles by a DMA were transported into a Single Particle Aerosol Mass Spectrometer (SPAMS), where the vacuum aerodynamic diameter and chemical composition of individual particles were measured. Size-resolved optical properties of biomass burning particles were also measured by Cavity Attenuated Phase Shift spectroscopy (CAPS). A thermodenuder (TD) was used to help analyze the mixing state of particles by removing the volatile compounds and leaving behind the less volatile species based on the vaporization temperature of materials. The purpose of our study was to add physicochemical knowledge regarding biomass burning particles which is an important aerosol source globally.

2 Experiments

2.1 Laboratory-made biomass burning particles

Rice straw, a typical type of crop residue in Southern China, was taken as the

representative biomass burning material in our experiment. The self-designed combustion setup was introduced in previous work (Huo et al., 2016). Briefly, the rice straws collected in rural residential area in Shanghai were dehydrated for 24 h at 100^{o}C in an oven prior to combustion. Five replicate tests of straw-burning were conducted for each experiment. For each test, ~ 50g of dried rice straws were burned in a combustion stove at a flaming condition. The emitted smoke was introduced into a 4.5 m^3 (in volume) chamber with a flowrate of 50 L/min. Ambient air was introduced though a high efficiency particulate air filters to maintain the ambient pressure. The particles in chamber were then introduced into the measurement system through a silica gel type diffusion drier (shown in Figure 1).

2.2 Single particle mass spectrometry

A Single Particle Aerosol Mass Spectrometer (SPAMS) (Hexin Analytical Instrument Co., Ltd) was deployed to examine the aerosol chemical composition and aerodynamic diameter at single-particle level. Detailed information on the SPAMS has been described elsewhere (Li et al., 2011). Briefly, particles in the size range of 0.2-2.0 μm are first drawn into the vacuum through an Aerodynamic Focusing Lens. Each particle is accelerated to a size-dependent aerodynamic velocity which is calculated based on two orthogonally oriented continuous lasers (Nd: YAG, 532 nm). The two lasers are fixed at a 6 cm distance and the delay of the scatter light is collected by two photomultiplier tubes (PMT). When a particle arrives at the ion source region, a pulsed desorption/ionization laser (Qswitched Nd: YAG, 266 nm) is triggered. Ions are recorded by a bipolar time-of-flight spectrometer, which records both positive and negative mass spectra for each single particle. In this work, the power of desorption /ionization laser was set to ~0.6 mJ per pulse. The aerodynamic diameter measurement is calibrated with curves generated by monodisperse polystyrene latex spheres (Nanosphere Size Standards, Duke Scientific Corp.) with known diameters (0.2-2.0 μm).

All single particle mass spectra acquired were converted to a list of peaks at each m/z by setting a minimum signal threshold of 30 arbitrary units above the baseline with TSI MS-Analyze software. The resulting peak lists together with other SPAMS data were imported into YAADA (version 2.11, www.yaada.org), a software toolkit for single-particle data analysis written in Matlab (version R2011b). In this work, a total of 10220 biomass burning particles were chemically analyzed according to their positive and negative ion spectra, accounting for about 48 % of all sized particles. According to the similarities of the mass-to-charge ratio and peak intensity, the biomass burning particles were classified using an adaptive resonance theory-based clustering method (ART-2a) (Song et al., 1999). Base on previous work (Huang et al., 2013; Spencer et al., 2007), parameters for ART-2a used in this work such as vigilance factor, learning rate, and iterations were 0.85, 0.05, and 20, respectively. The particle clusters resulting from ART-2a were then grouped into 6 particle types based on the mass spectral patterns and chemical similarities. The name of a particle type reflects the dominant chemical species.

2.3 Effective density measurements

2.3.1 Theoretical calculation and methods

Particle density (ρ_p) is referenced to the volume equivalent diameter (d_{ve}) which is defined as the diameter of a spherical particle with the same volume as the particle under consideration. Particle density can be derived as follows, where m_p is the particle mass:

$$\rho_p = \frac{m_p}{\frac{\pi}{6} {d_{ve}}^3} \quad (1)$$

When particles are not spherical, the "effective density", not necessarily a true measurement of particle density is derived. Various definitions of effective density are provided in the literature, and a review of these definitions is given by DeCarlo et al. (2004). Different definitions may aim to present different values for a given particle. It is important to understand the derivation, calculation, and measurement for one method of particle effective density.

(1) DMA-APM-CPC system

The effective density of a particle can be calculated by combining mobility and mass measurements under the assumption that the particle is spherical, thus its physical diameter equals to the electrical mobility diameter (d_m) measured by a DMA. The effective density (ρ_{eff}^{I}) can be calculated by the following equation:

$$\rho_{eff}^{I} = \frac{m_p}{\frac{\pi}{6} {d_m}^3} \quad (2)$$

where m_p stands for particle mass obtained by an APM. In our work, we selected biomass burning particles with mobility diameters of 50 nm, 100 nm, 200 nm, and 400 nm and determined their effective density using the DMA-APM-CPC system.

(2) DMA-SPAMS system

Another approach of deriving effective density is through a combination of mobility and aerodynamic measurements. Simultaneously measuring the particle electrical mobility diameter (d_m) by DMA and the vacuum aerodynamic diameter (d_{va}) by SPAMS allows for the determination of particle effective density (ρ_{eff}^{II}) by the following equation:

$$\rho_{eff}^{II} = \frac{d_{va}}{d_m} \rho_0 \quad (3)$$

where ρ_0 is the standard density (1.0 g/cm^3). In this study, since particles smaller than 200 nm may not scatter sufficient light to be detected by SPAMS and the number concentration of biomass burning particles above 400 nm was low (shown in Figure S1), we selected 200 nm and 400 nm particles by DMA and then introduced them into SPAMS.

(3) Shape factor calculation

The shape of particles can influence the optical properties and can reflect the mixing state of particles to some degree. It is possible to extract the shape information

based on the measurements above.

The relationship between the volume equivalent diameter (d_{ve}) and mobility diameter (d_m) is shown in the following equation:

$$\frac{d_m}{C_c(d_m)} = \frac{d_{ve}\chi}{C_c(d_{ve})} \quad (4)$$

where χ is the shape factor, the ratio of the resistance force on the nonspherical particle to the resistance force on its volume equivalent sphere (Hinds, 1999). The χ value equals 1 for spherical particles and is greater than 1 for nonspherical/irregular particles.

Cc is the Cunningham Slip Correction Factor parameterized as:

$$Cc(d) = 1 + \frac{2\lambda}{d}[\alpha + \beta\exp(-\gamma\frac{d}{2\lambda})] \quad (5)$$

where d is the particle diameter (d_m or d_{ve}) and λ is the mean free path of gas molecules. The empirical constants α, β, and γ are 1.142, 0.558, and 0.999 respectively (Allen and Raabe, 1985).

The vacuum aerodynamic diameter (d_{va}) is related to the volume equivalent diameter (d_{ve}) by:

$$d_{va} = \frac{\rho_p}{\rho_0}\frac{d_{ve}}{\chi} \quad (6)$$

As the measurements of mobility and aerodynamic diameters are readily available, we assumed the error was in the particle mass measurement if the measured $\rho_{eff}^{//}$ is used to replace $\rho_{eff}^{/}$ in Equation (2) (Decarlo et al., 2004). With assumed particle density (ρ_p) and known particle mass (m_p) measured by an APM, a calculated d_{ve} could be obtained using Equation (1). Though ρ_p was unknown, it would be canceled out later. Using the same d_{ve} and for any shape factor (χ), a calculated d_m and d_{va} was obtained by Equation (4) and (6), respectively. Thus, $\rho_{eff}^{//}$ could be obtained by the calculated d_m and d_{va} and an estimated m_p was calculated by replacing $\rho_{eff}^{/}$ by $\rho_{eff}^{//}$ in Equation (2). We then calculated the ratio of the estimated m_p to the exact m_p as a function of d_m and χ (shown in Figure S5, discussed in Section 3.1.5).

2.3.2 Instrumentation for effective density measurements

The size distribution of biomass burning particles was detected by a Scanning Mobility Particle Sizer (SMPS) consisting of a Differential Mobility Analyzer (DMA, Model 3080, TSI Inc.) and a Condensation Particle Counter (CPC, Model 3775, TSI Inc.). An Aerosol Particle Mass analyzer (APM, Model 3601, Kanomax Inc.) was used to classify aerosol particles according to their mass-to-charge ratio. The detailed information of the APM classification principle was previously reviewed by Tajima et al. (2011). Briefly, particles were size-selected by DMA after being charged with a Kr-85 neutralizer. Particles with a known size were then introduced into APM. When the radial electrical and centrifugal forces were in balance, particles passed through

the rotating cylinders to CPC. Mass distribution was obtained by voltage scanning and particle counting.

2.4 Optical measurements

Cavity Attenuated Phase Shift (CAPS) spectroscopy (Shoreline Science Research Inc.) was used to determine the particle extinction and scattering coefficient. Detailed information on the CAPS is available in Onasch et al. (2015). Briefly, a square-wave modulated light-emitting diode (LED) is transmitted through an optical cavity cell. A sample cell incorporating two high reflectivity mirrors (R~0.9999) with a vacuum photodiode detector (Hamamatsu R645) centers at the wavelength of the LED. The particle extinction coefficient [$b_{ext}(\lambda)$] can be obtained from the changes in the phase shift of the distorted waveform of the LED. An integrating nephelometer using a 10 cm diameter integrating sphere is operated to measure the scattering coefficient [$b_{scat}(\lambda)$]. Particles are illuminated by the collimated light beam which has measured the extinction. The scattered light of particles is collected at all angels by the integrating sphere. A PMT (H7828-01, Hamamatsu) with a high voltage power supply and an amplifier records the scattered light. In this work, we used two CAPSs with the LED light sources at wavelength of 450 nm and 530 nm to detect the optical properties of biomass burning particles, respectively.

2.5 Thermodenuder

A thermodenuder (TD, Model 3065, TSI Inc.) was utilized to separate volatile and less volatile species of biomass burning particles at specific temperatures. The TD consists of a 40 cm long desorber section and a 70 cm long adsorption tube. The sample can be heated up to 400 ^{o}C in the desorber section while we selected 150 ^{o}C and 300 ^{o}C in this work. The adsorption tube is surrounded by an annular bed of activated carbon which adsorbs the evaporated gas-phase compounds, leaving behind the less volatile fractions. With a flowrate of 0.6 L/min, the residence time of particles in the TD heating section was approximately 9 s in this work.

The particle number fractions after heating do not necessarily represent the actual number fractions before heating as some of the particles can evaporate completely. Besides, particle loss could be produced both in the TD heating and adsorption section due to thermophoretic forces and diffusion, respectively (Philippin et al., 2004). On account of the quantitative measurements of optical properties, particle loss could lead to the underestimate of b_{ext} and b_{scat}.

Sodium chloride (NaCl) aerosol produced by a single-jet atomizer (Model 9302, TSI Inc.) was used to determine the transport efficiency (η) in TD. The transport efficiencies of NaCl of different electric mobility diameters selected by DMA (d_m: 50, 100, 200, and 400 nm) at a range of temperatures (T_i: 20, 150, and 300 ^{o}C) are shown in Figure S2. In TD, η decreased with increasing T_i and decreasing d_m, which is consistent with the result in Philippin et al. (2004). The measured η were used to correct the particle number concentration in the calculation of all the measurements related to the thermal-denuded process.

2.6 Shrink factor

The thermal-denuded method to separate the coating of particles for absorption enhancement calculation as well as other experiments related to particle volatility has been used in previous work (Nakayama et al., 2014; Chan et al., 2011; Lack et al., 2012). However, particles might shrink to smaller sizes after thermal treatment. The particle shrinkage should be taken into consideration for size-selected volatility experiments which was neglected in previous work. The major reason could be the extremely low concentration for size-selected particles after thermal-denuded process up to 300 ^{o}C. The concentration of the size-selected particles was too low to be detected in the following instruments.

Therefore, we developed an approximation of the particle shrinkage calculation. A tandem DMAs (TDMA) was utilized to detect the size change of particles. Here, we used the ratio of the particle diameter after heating (d_{m2}) to the diameter before heating (d_{m1}) as the shrink factor (d_{m2}/ d_{m1}) of particles (shown in Figure S3). An approximation of the peak value for the dominant shrink factor mode was used for each diameter. The selection of particle diameter after thermal-denuded process was based on the original dried-particle diameter multiplied the shrink factor of each diameter (discussed in supplementary).

3 Result and discussion

3.1 Size-resolved effective density

3.1.1 Effective density from DMA-APM-CPC measurements (ρ_{eff}^{I})

The effective density of particles, measured using the DMA-APM-CPC system (ρ_{eff}^{I}), provided useful information on the mixing state of particles. A Gaussian model was applied to determine the effective densities of the biomass burning particles selected by DMA (shown in Figure 2). The density distribution of 50 nm (d_m) particles showed a single peak profile with a peak value of 1.17 g/cm^3 (Table S1). Two possible factors could be inferred from this feature: a nearly-monodisperse aerosol effective density distribution or a juncture of two modes with very close peak values. Biomass burning particles contain highly agglomerated structures like soot (Martins et al., 1998). Although the material density of black carbon (BC) is ~1.8 g/cm^3 (Bond and Bergstrom, 2006), fresh BC particles with an aggregate structure can have an effective density less than 1.0 g/cm^3 (Rissler et al., 2014). The density of organic matter varies in the range of 1.2-2.0 g/cm^3 depending on sources (Hand et al., 2010; Turpin and Lim, 2001). Since particles of 50 nm have the possibility of containing organic matter rather than BC alone, the apparent single-peak density distribution of these particles was more likely due to the combination of two modes representing BC and organic particles respectively (as the dash lines shown in Figure 2). The thermal desorption method can help to explain the mixing state of 50 nm particles which will be discussed in Section 3.1.3.

The density distribution of 100 nm particles exhibited a peak at 1.45 g/cm^3 at room temperature, which suggests that these particles were dominated by organic

matter. However, less-massive composition with effective density of 0.9-1.1 g/cm^3 was also obtained for 100 nm particles. This range is identical with the density of fresh BC with aggregate structure. The bi-modal distribution of the density profile of 100 nm particles suggests that BC was partly externally mixed with other components in ultrafine particles from biomass burning emissions. Similar result has been found by Lack et al. (2012) and Adachi et al. (2011). The external mixing of BC and organic particulate matter was evident in the density distribution of 200 nm particles as well (Figure 2). For 400 nm particles, besides a dominant density mode at 1.34 g/cm^3, a relative weak mode with effective density of 1.92 g/cm^3 was observed. Previous studies have shown that potassium chloride crystals, which have a material density of ~ 1.99 g/cm^3 (Lide, 2008), were observed in the TEM of fresh biomass burning particles (Li et al., 2015). Evidence of external mixing sodium and potassium salts in ambient environment was also observed by single particle mass spectrometry in previous work (Zauscher et al., 2013; Bi et al., 2011). A recent work performed by Lee et al. (2016) reported that K^+ was not uniformly mixed in biomass burning particles with less than 20% particles containing high K^+ content. Thus, we estimate that the mode at 1.92 g/cm^3 was associated with KCl, and possibly KSO_4 and KNO_3, and that these crystalline species were more likely externally mixed with organic matter in biomass burning particles. The similar results of the externally mixed aerosol population was observed by Moffet et al. (2008) with a wide range of densities (1.1-3.4 g/ cm^3).

Though freshly emitted, biomass burning particles can be coated by secondary species, such as ammonium nitrate and ammonium sulfate, pronouncedly in a very short period (Leskinen et al., 2007). The bulk densities of ammonium nitrate and ammonium sulfate are ~1.75 g/cm^3. The differences in the peak values of the dominant mode observed for 50-400 nm particles are associated with the composition and morphology of particles. Different proportions of the same material can lead to differences in particle effective density. The dominant modes for biomass burning particles in the size range of 50-400 nm (Figure 2) could be a mixture of similar composition (BC, OC, potassium salts and secondary inorganic species) but different proportions. Detailed information and discussion about the particle composition can be found in Section 3.2.

3.1.2 Effective density from DMA-SPAMS measurements (ρ_{eff}^{II})

The vacuum aerodynamic size distributions of 200 nm and 400 nm electrical mobility selected biomass burning particles are shown in Figure 3. The dominant mode for the 200 nm mobility selected particles was 280 nm in vacuum aerodynamic diameter with an effective density (ρ_{eff}^{II}) of 1.40 g/cm^3 and a second mode at 360 nm (d_{va}) with an effective density of 1.80 g/cm^3. This is quite consistent with the result from the DMA-APM-CPC method. The less intense mode at 520 nm (d_{va}) should be due to doubly charged particles (Spencer et al., 2007). For 400 nm mobility selected particles, the dominant mode in aerodynamic diameter was 540 nm with an effective density of

1.35 g/cm^3. Since the less massive modes at 660 nm and 840 nm were not in the range of doubly charged particles, these two modes were singly charged particles with effective density of 1.65 and 2.10 g/cm^3, respectively. The single-particle level chemical composition of biomass burning particles will be discussed below.

Figure S4 summarizes that the average effective densities (ρ_{eff}^{I} & ρ_{eff}^{II}) of biomass burning particles that were size-selected at 6 different mobility diameters. Note that the density distributions of the 300 nm and 350 nm (d_m) particles are not contained in Figure 2 since they were similar to those of the 200 nm and 400 nm (d_m) particles. The 50 nm biomass burning particles had the lowest effective density of 1.15 ± 0.23 g/cm^3 which could be due to the aggregate structure of black carbon. Compared with 50 nm (d_m) particles, the effective density of 100 nm particles was higher (1.45 ± 0.15 g/cm^3). Since the sampling limitation of SPAMS was 200 nm, ρ_{eff}^{II} was derived only for particles in the size range of 200-400 nm (d_m). Overall, these two methods had consistent results. The differences between the average values from the two methods were less than 8% for all particle sizes. We noticed that ρ_{eff}^{II} were generally smaller than ρ_{eff}^{I}, which could be due to the systematic error from different measurements.

3.1.3 Thermal-denuded particle effective density

The average density distributions of 50-400 nm (d_m) biomass burning particles after heating at 150^{o}C and 300 ^{o}C, respectively, are shown in Figure 2. It is worth noting that the thermal-denuded particle density distribution here was not from the particles with the same original dried-particle diameter. However, our observations are still meaningful since the evolution trends of density distribution after heating were similar despite of the particle size.

After heating by TD, the bi-modal density distributions of biomass burning particles became more pronounced. At 150 ^{o}C, the effective density mode with peak at ~1.0 g/cm^3 protruded for the whole size range of 50-400 nm particles. The separation of the peaks after heating suggested that the some less volatile BC or soot with effective density of ~1.0 g/cm^3 was possibly externally mixed with other compositions. The dominant density peak values for 50, 100, 200, and 400 nm particles at 150 ^{o}C were 1.64-1.80 g/cm^3. Li et al. (2016) reported that the density of organic matter vaporized at 150 ^{o}C was 0.61-0.90 g/cm^3. The increase of the dominant density peak value (1.34-1.45 g/cm^3 for unheated vs. 1.64-1.80 g/cm^3 for 150 ^{o}C heated) could be due to the volatilization of organics with low effective density. The dominant density peak values of 50-400 nm particles at 300 ^{o}C were 1.75-2.04 g/cm^3. The volatilization temperatures of ammonium nitrate and ammonium sulfate are reported to be ~48-89 ^{o}C and ~178-205 ^{o}C, respectively (Johnson et al., 2004a; Johnson et al., 2004b). Thus, the fractions of ammonium nitrate and ammonium sulfate should be small at 300 ^{o}C. The increase of dominant density peak value for 50-400 nm biomass burning particles upon heating could be due to the vaporization of

volatile organics with low effective density and secondary inorganic species such as NH_4NO_3 and $(NH_4)_2SO_4$ with density of ~1.75 g/cm^3. Besides, Bond and Bergstrom (2006) reported that the density of light-absorbing carbon should be 1.7-2.1 g/cm^3 which is quite high compared with the density of the volatile organics (0.61-0.90 g/cm^3). Saleh et al. (2014) had shown that the light-absorbing organics in biomass burning particles were extremely low volatility organic compounds. Thus, we assume these extremely low volatility organics should play an important role in the dominant effective density mode at 300^{o}C.

Upon heating, the density mode of KCl and partly K_2SO_4 at ~2.0 g/cm^3 was ambiguous as the dominant mode shifted right and overlapped with the KCl mode (dash lines shown in Figure 2). However, at 300 ^{o}C, the dominant mode of 400 nm particles was at 2.05 g/cm^3 which fitted the density of potassium salts, indicating the main material of 400 nm heated (~800 nm unheated, detected by a tandem DMAs) biomass burning particles should be potassium salts with vaporization temperatures above 700 ^{o}C (Knudsen et al., 2004).

With heating by TD, the aerodynamic size distributions of 200 nm and 400 nm electrical mobility size-selected biomass burning particles at 300 ^{o}C are shown in Figure 3. The increase of ρ_{eff}^{II} upon heating was consistent with that of ρ_{eff}^{I}.

3.1.4 Shape factor

The shape of particles has been suggested to play an important role in their optical properties (Zhang et al., 2008) and mixing state (China et al., 2013). Shape factor was introduced to account for the ratio of the drag forces on a particle due to nonspherical/irregular shape. Shape factor, which can be extracted based on the measurement of particle density and mass has been introduced in Section 2.3.1.

We calculated the ratio of the estimated m_p to the exact m_p as a function of d_m and χ (shown in Figure S5). For nonspheical particles ($\chi > 1$), the estimated mass was larger than the actual mass. We calculated the estimated mass using the exact ρ_{eff}^{II} measured by the DMA-SPAMS to replace the ρ_{eff}^{I} in Equation (2) as well. The ratios of the estimated mass by this mean to the exact mass for 200, 300, 350, and 400 nm mobility selected particles were 1.4, 1.3, 1.3, and 1.2 respectively (red dots in Figure S5). Thus, we could estimate the χ of the particle measured using the DMA-SPAMS in the size range of 200-400 nm. Totally, the χ of 200-400 nm biomass burning particle in this work exceeded 1.2 (~1.2-2.2). The χ decreased with the increase of d_m while the effective density showed the same trend. The more regular shape and lower effective density of 400 nm particles compared with that of 200 nm particles could be due to the particle chemical composition and particle voids (discussed in Section 3.2).

3.2 Size-resolved chemical composition

The mass spectra of individual biomass burning particles have been studied in previous work (Silva et al., 1999; Zauscher et al., 2013). Based on the mass spectra of

single particles, the biomass burning particles were classified into 6 particle types: 1) BB-CN: biomass burning (BB) particles with a strong CN^- (*m*/*z* -26 [CN^-]) peak; 2) BB-EC: BB particles with strong elemental carbon clusters ($C_n^{+/-}$); 3) BB-Nitrate: BB particles with strong nitrate (*m*/*z* -46[NO_2^-], -62[NO_3^-]) signals; 4) BB-Sulfate: BB particles with strong sulfate (*m*/*z* -97[HSO_4^-]) signals; 5) BB-KCl: BB particles with strong potassium chlorine (*m*/*z* 113[K_2Cl^+]) signals; and 6) BB-OC: BB particles with strong organic carbon peaks (e.g., *m*/*z* 27[$C_2H_3^+$], 37[C_3H^+], 43[$C_3H_7^+$], 51[$C_4H_3^+$], et al.). The naming of the chemical classes is based on some of the dominant chemical species in an attempt to keep the names short. The mass spectra for each particle type are presented in Figure S6. The percentages of 6 particle types in different modes of aerodynamic size distribution for 200 nm and 400 nm mobility selected particles are shown in Figure 3. For 200 nm mobility selected particles, the dominant particle types were BB-EC and BB-CN. The percentages of particle types within the two aerodynamic modes differ slightly. Compared with the first mode, the second mode contains more BB-CN (24.4% vs. 29.6%), more BB-KCl (1.0% vs. 4.3%) and less BB-EC (32.2% vs. 22.9%). We supposed that the density of each particle type largely depended on the dominant species. The exact effective density of each particle type could not be obtained directly while the relative value compared with other particle types could be inferred from the material density of dominant species. For example, the BB-KCl type might have higher effective density compared with others since the dominant composition KCl has a material density of ~1.99 g/cm^3 (Lide, 2008). The increased BB-KCl type and the decrease of BB-EC (~1.0 g/cm^3) resulted in a higher effective density in the second mode than the first mode.

The fractional distributions of the 6 particle types for 200 nm and 400 nm mobility selected particles were apparently different (Figure 3). For 400 nm mobility selected particles, the proportions of BB-Nitrate, BB-Sulfate and BB-KCl types were larger than those of 200 nm mobility selected particles. The dominant chemical species for BB-Nitrate and BB-Sulfate particle types could be NH_4NO_3 and $(NH_4)_2SO_4$ with material density of ~1.75 g/cm^3 (Lide, 2008). Compared with other types, BB-Nitrate, BB-Sulfate and BB-KCl were particle types with higher density. However, the effective density for 400 nm mobility selected particles was lower than that of 200 nm. In addition to the compositional differences, particle morphology could be another reason responsible for the observed differences in the effective densities between these two sizes. Indeed, it has been found that the morphology like void ratio, particle shape factor, and fractal dimension of particles all greatly affect particle effective density (DeCarlo et al., 2004). Though the shape factor discussed in Section 3.1 had shown that the 400 nm (d_m) particles had a more spherical morphology, their lower average effective density compared to smaller particles could be due to the voids in particles. Amorphous species such as NH_4NO_3 (Audebrand et al., 1997) could lead to the low effective density of particles. Thus, we supposed the lower effective density of 400 nm particles compared with 200 nm particles was caused by the large proportion of NH_4NO_3 and $(NH_4)_2SO_4$ with fluffy material properties.

For 400 nm mobility selected particles, the pie charts of particle type were

almost identical for the first and second modes (as shown in Fig. 3b, 20 ^{o}C). Thus, we assume these two modes were derived from one effective density mode. The proportion of BB-KCl in the third mode at 840 nm with effective density of 2.10 g/cm^{3} greatly increased compared with the first two modes (8.8%, 9.2% vs. 32.7%). The increased BB-KCl indicated that the KCl crystals were external mixed and tended to be mixed with larger size particles which were consistent with the DMA-APM-CPC result.

Upon heating by TD, the proportions of BB-CN and BB-KCl increased, indicating that these types of particles were composed of less volatile species (shown in Figure 3) (Zhai et al., 2015). At 300^{o}C, the fractions of BB-Nitrate and BB-Sulfate decreased, consistent with the volatilization temperature ranges of ammonium nitrate (~48-89 ^{o}C) and ammonium sulfate (~178-205 ^{o}C) (Johnson et al., 2004a; Johnson et al., 2004b). The high effective density (>2.0) of biomass burning particles at 300^{o}C could be due to the vaporization of volatile organics with low density since the BB-OC type decreased drastically after thermal treatment. Besides, the increasing proportion of BB-KCl upon heating could be another important reason for the higher effective density at 300 ^{o}C.

3.3 Size-resolved optical properties

3.3.1 Single scattering albedo (SSA)

The single scattering albedo (SSA), was calculated using the following equation:

$$SSA\ (\lambda) = b_{scat}\ (\lambda) / [b_{abs}\ (\lambda) + b_{sca}\ (\lambda)]$$

where b_{scat} is the particle light scattering coefficient, b_{abs} is the light absorption coefficient, and λ is wavelength. The light scattering and extinction coefficients (b_{ext}, = b_{abs} + b_{sca}) for biomass burning particles in this work were measured at 530 nm and 450 nm wavelengths using CAPSs.

The size-resolved SSAs for biomass burning particles are shown in Figure 4. Totally, the SSAs for biomass burning particles in the mobility size range of 50-400 nm varied narrowly. It's worth noting that the optical measurement was based on bulk measurement by CAPSs, which is not sensitive to the diversity of particle mixing state.

The SSA (530 nm) for 50 nm particles was the lowest (0.889±0.006) as the percentage of strong light-absorbing black carbon for particles in this size range was larger (shown in Figure 3, discussed in Section 3.2). For 100-400 nm biomass burning particles, the SSAs were relatively steady (0.897±0.006 - 0.900±0.006).

The size-resolved SSAs at 450 nm (λ) for biomass burning particles were generally lower than those at 530 nm (λ). Previous studies have shown that biomass burning was an important source of brown carbon (BrC) which is light-absorbing in the UV-vis range (Lack and Cappa, 2010). For 50 nm (d_m) particles, the SSA (λ=450 nm) was also the lowest, due to the dominance of the strong light-absorbing BC in these particles. However, unlike the trend of size-resolved SSAs (λ=530 nm), the SSA (λ=450 nm) of 100-400 nm particles increased as the size increased. It has been shown that brown carbon arising from biomass burning is primarily composed of extremely low volatility organic compounds (Saleh et al., 2014). The CN^{-} in biomass

burning particles is representative for some extremely low volatility nitrogen-containing organics (Zhai et al., 2015). As shown in Figure 3, compared with 400 nm particles, the proportion of organic matter (BB-CN, BB-OC) was larger for 200 nm particles. The nitrogen-containing species might indicate the existence of light-absorbing organics. The lower SSA (λ=450 nm) for 200 nm particles might indicate a larger proportion of BrC. We assumed the lower SSA (λ=450 nm) for 100 nm performed in a similar way with a larger proportion of BrC.

3.3.2 Ångström absorption exponent (AAE)

To investigate the wavelength dependence of the absorption coefficients, we determined the Ångström absorption exponent (AAE) based on absorption measurements at two different wavelengths (λ_1 & λ_2) using the following equation:

$$AAE\ (\lambda_1 / \lambda_2) = - \ln[\ b_{abs}\ (\lambda_1) / b_{abs}\ (\lambda_2)] / \ln(\lambda_1 / \lambda_2)$$

The AAE in this work was calculated from the light absorption coefficients at wavelengths of 450 nm and 530 nm measured by the CAPSs. The uncertainties in the calculated AAE values can be caused by the uncertainties in the calibration factors of CAPSs. The size-resolved AAEs for biomass burning particles are shown in Figure 4. Black carbon is highly absorbing in the visible spectrum with little variation with wavelength and shows an AAE of ~1.0 (Bergstrom et al., 2002). As brown carbon species absorb light in the UV-vis range, BrC-containing particles usually exhibit an AAE above 1 (Martinsson et al., 2015). Lack and Cappa (2010) used modeling to calculate AAE values and suggested that particles with AAE exceeding 1.6 should be classified as BrC. In our study, the AAE values of particles in the size range of 50-400 nm were higher than 1.6, indicating that they were BrC-containing particles from biomass burning. Among all sizes, the AAE of 50 nm biomass burning particles was the lowest (~5.8) while that of 100 nm particles was the highest (~6.3). The main light-absorbing functional groups in the UV-vis range is conjugated double bond (Laskin et al., 2015). BB-CN and BB-OC particle types identified by mass spectra in our work tended to contain more large molecules of BrC with light-absorbing functional groups. We noticed that the proportion of BB-OC type species was larger in 200 nm particles (Figure 3) and with higher AAE value, compared with 400 nm particles. Thus, we suppose the highest AAE value observed for 100 nm particles might be the result of the largest BrC proportion.

The SSA and AAE values of total biomass burning particles are shown in Table S2. The decrease of SSA values upon heating was due to the vaporization of secondary inorganic species like NH_4NO_3 and less absorbing organics. The AAE values for all particles at 150 ^oC and 300 ^oC were ~19% and ~64%, lower than those at room temperature (20 ^oC). The significant decrease of AAE at 300 ^oC could be due to the vaporization of light-absorbing organics in the temperature range of 150-300 ^oC. However, the AAE value at 300 ^oC was still above 1.6, indicating the presence of extremely low volatility light-absorbing organics in biomass burning particles. McMeeking et al. (2014) found that the strongly light-absorbing biomass burning particles tended to have a weak wavelength dependent absorption while the weakly light-absorbing particles tended to have a strong wavelength dependent absorption,

which is consistent with our results. In this work, the high values of AAE (~ 6.23) and SSA (~0.89, at 530 nm) suggested the light absorbing of rice straw burning particles were relatively weak compared to the particles emitted from other types of biofuels.

3.3.3 Absorption enhancement (E_{abs})

The impact of other particle components on BC absorption, either internally or externally mixed of BC with organic aerosol and inorganic salts, has drawn significant attention. The light absorption by an absorbing core can be enhanced when coated with a purely scattering shell which acts as a lens. Absorption enhancement has been observed in laboratory for BC particles coated with various materials (Schnaiter et al., 2005; Zhang et al., 2008), and in field observation (Schwarz et al., 2008; Spackman et al., 2010). Previous studies have reported the absorption enhancement values in a range of 1.2-1.6 for biomass burning particles (Moffet and Prather, 2009; McMeeking et al., 2014). However, some other studies suggested that BC absorption enhancement due to lensing is minimal and climate models might overestimate the warming effect by BC (Healy et al., 2015; Cappa et al., 2012). In this study, we measured the absorption enhancement of freshly emitted straw combustion particles.

The light absorption enhancement (E_{abs}) due to coating was estimated by the ratio of $b_{abs}(\lambda)$ for particles that did and did not pass through the TD:

$$E_{abs}(\lambda, T) = b_{abs}(\lambda, T_0) / b_{abs}(\lambda, T)$$

where T is the TD temperature (150 or 300 ^{o}C), T_0 is the room temperature (20 ^{o}C in this work). The absorption coefficient of particles was calibrated by the transport efficiency of TD and shrink factor of each diameter as mentioned in Section 2.5 and 2.6.

The size-resolved E_{abs} observed at wavelengths of 530 nm and 450 nm are shown in Figure 5. Though freshly emitted, absorption enhancements (E_{abs}) of biomass burning particles in the size range of 50-400 nm were observed (E_{abs} >1). Totally, the E_{abs} increased with increasing particle diameters with the largest E_{abs} (λ=530 nm) of 1.197±0.082 and the E_{abs} (λ=450 nm) of 1.460±0.101 for 400 nm particles. One possible reason could be explained by the thicker coating (both primary and secondary organic and inorganic species) for larger particles. Other than coating thickness, absorption enhancement of particles could be related with the mixing state and morphology (Liu et al., 2015). The E_{abs} (λ=450 nm) were overall larger than the E_{abs} (λ=530 nm). You et al. (2016) reported that the E_{abs} of BC internally mixed with humic acid (HA/BC) ranged from 2 to 3 and was strongly wavelength dependent. Removal of the HA absorption contribution revealed the independence of wavelength. Thus, the larger E_{abs} (λ=450 nm) in this work could be due to the absorption of light-absorbing organics.

4 Conclusions

As a major primary source of aerosols, biomass burning emissions significantly impact the global radiative budget. It is important to understand the physical and chemical properties of biomass burning particles, as well as their links to optical

properties. In this work, rice straw was combusted as a representative material of biomass burning in Southern China. A series of comprehensive methods was used to detect the size-resolved chemical composition, effective density, and optical properties of the particles emitted from the burns.

Two methods were utilized to measure the effective density of the biomass burning particles. The DMA-APM-CPC system, which has been widely used in chamber and field work, offered size-resolved information on the particle effective density. The DMA-SPAMS system provided physical property and chemical composition at single-particle level. The 50 nm (d_m) biomass burning particles had the lowest effective density of 1.15 ± 0.23 g/cm^3, which was due to the large proportion of fractal black carbon. The apparent single-peak density distribution of 50 nm particles was due to the combination of two modes (BC and organic matter, respectively). The independent modes at 0.9-1.1 g/cm^3 shown in the density distribution of 100 nm and 200 nm particles and ~1.92 g/cm^3 mode shown in that of 400 nm particles indicated that BC and crystalline species such as KCl in fresh biomass burning particles tended to be externally mixed with organic carbon. With heating by TD, the separation of the effective density distribution modes testified the presence of BC, potassium salts and less volatile OC in the biomass burning particles.

The effective density measured by DMA-SPAMS system was consistent with the result by DMA-APM-CPC method. The dominant modes in the effective density distributions of 200 nm and 400 nm mobility selected particles were 1.40 g/cm^3 and 1.35 g/cm^3, respectively. The crystalline KCl with an effective density of 2.10 g/cm^3 (with BB-KCl type accounting for 32.7%) was observed in the density distribution for 400 nm particles measured by DMA-SPAMS. The proportions of BB-Nitrate, BB-Sulfate, and BB-KCl types in 400 nm mobility selected particles were larger than those in 200 nm mobility selected particles. Compared with 200 nm particles, 400 nm particles showed more spherical morphology but lower effective density, which could be due to the larger proportion of low density organics and amorphous NH_4NO_3.

The size-resolved extinction and scattering coefficients were measured by CAPSs at wavelengths of 450 nm and 530 nm. The SSA (λ=530 nm) for 50 nm particles was the lowest (0.889 ± 0.006) because of the presence of a larger percentage of the strongly light-absorbing black carbon particles in this size mode. The size-resolved SSAs (λ=450 nm) for biomass burning particles were generally lower than the SSAs (λ=530 nm). The AAE values in the size range of 50-400 nm particles were all above 1.6, indicating the significant presence of brown carbon in all sizes. The AAE value was the lowest for 50 nm particles (~5.8) while was the highest for 100 nm particles (~6.3). Compared with 400 nm particles, the proportions of BB-OC and BB-CN, the extremely low volatility organic compounds, were larger for 200 nm particles which might indicate a higher possibility for the existence of light-absorbing organics. The E_{abs} was observed in freshly emitted biomass burning particles. The E_{abs} increased with larger diameter which might be due to increasing coating thickness. The wavelength-dependent E_{abs} of particles were likely due to the absorption of light-absorbing organics. Our work emphasizes on the complex mixing states of aerosols from primary source. Further research on how particle morphology affects

the optical properties of biomass burning particles is needed.

Acknowledgements

This work was supported by the National Natural Science Foundation of China (91544224, 21507010), the Ministry of Science & Technology of China (2012YQ220113-4), the Science & Technology Commission of Shanghai Municipality (14DZ1202900), and the Changjiang Scholars program of the Chinese Ministry of Education.

References

Adachi, K., and Buseck, P. R.: Atmospheric tar balls from biomass burning in Mexico, J. Geophys. Res.-Atmos., 116, doi:10.1029/2010jd015102, 2011.

Allen, M. D., and Raabe, O. G.: Slip correction measurements of spheical solid aerosol-particles in an improved millikan apparatus, Aerosol Sci. Technol., 4, 269-286, doi:10.1080/02786828508959055, 1985.

Andreae, M. O., and Merlet, P.: Emission of trace gases and aerosols from biomass burning, Global Biogeochem. Cy., 15, 955-966, doi:10.1029/2000gb001382, 2001.

Audebrand, N., Auffredic, J. P., and Louer, D.: Thermal decomposition of cerous ammonium nitrate tetrahydrate studied with temperature-dependent X-ray powder diffraction and thermal analysis, Thermochim. Acta, 293, 65-76, doi: 10.1016/s0040-6031(97)00064-6, 1997.

Barone, T. L., Lall, A. A., Storey, J. M. E., Mulholland, G. W., Prikhodko, V. Y., Frankland, J. H., Parks, J. E., and Zachariah, M. R.: Size-resolved density measurements of particle emissions from an advanced combustion diesel engine: effect of aggregate morphology, Energ. Fuel., 25, 1978-1988, doi:10.1021/ef200084k, 2011.

Bergstrom, R. W., Russell, P. B., and Hignett, P.: Wavelength dependence of the absorption of black carbon particles: Predictions and results from the TARFOX experiment and implications for the aerosol single scattering albedo, J. Atmos. Sci., 59, 567-577, doi: 10.1175/1520-0469(2002)059<0567:wdotao>2.0.co;2, 2002.

Bi, X. H., Zhang, G. H., Li, L., Wang, X. M., Li, M., Sheng, G. Y., Fu, J. M., and Zhou, Z.: Mixing state of biomass burning particles by single particle aerosol mass spectrometer in the urban area of PRD, China, Atmos. Environ., 45, 3447-3453, doi: 10.1016/j.atmosenv.2011.03.034, 2011.

Bond, T. C., Streets, D. G., Yarber, K. F., Nelson, S. M., Woo, J.-H., and Klimont, Z.: A technology-based global inventory of black and organic carbon emissions from combustion, J. Geophys. Res- Atmos., 109, doi: 10.1029/2003jd003697, 2004.

Bond, T. C., and Bergstrom, R. W.: Light absorption by carbonaceous particles: An investigative review, Aerosol Sci. Technol., 40, 27-67, doi: 10.1080/02786820500421521, 2006.

Bond, T. C., Doherty, S. J., Fahey, D. W., Forster, P. M., Berntsen, T., DeAngelo, B. J., Flanner, M. G., Ghan, S., Karcher, B., Koch, D., Kinne, S., Kondo, Y., Quinn, P. K., Sarofim, M. C., Schultz, M. G., Schulz, M., Venkataraman, C., Zhang, H., Zhang, S., Bellouin, N., Guttikunda, S. K., Hopke, P. K., Jacobson, M. Z., Kaiser, J. W.,

703 Klimont, Z., Lohmann, U., Schwarz, J. P., Shindell, D., Storelvmo, T., Warren, S.
704 G., and Zender, C. S.: Bounding the role of black carbon in the climate system: A
705 scientific assessment, J. Geophys. Res- Atmos., 118, 5380-5552, doi:
706 10.1002/jgrd.50171, 2013.
707 Cao, G., Zhang, X., Wang, Y., and Zheng, F.: Estimation of emissions from field
708 burning of crop straw in China, Chinese Sci. Bull., 53, 784-790, doi:
709 10.1007/s11434-008-0145-4, 2008.
710 Cappa, C. D., Onasch, T. B., Massoli, P., Worsnop, D. R., Bates, T. S., Cross, E. S.,
711 Davidovits, P., Hakala, J., Hayden, K. L., Jobson, B. T., Kolesar, K. R., Lack, D. A.,
712 Lerner, B. M., Li, S. M., Mellon, D., Nuaaman, I., Olfert, J. S., Petaja, T., Quinn, P.
713 K., Song, C., Subramanian, R., Williams, E. J., and Zaveri, R. A.: Radiative
714 Absorption Enhancements Due to the Mixing State of Atmospheric Black Carbon,
715 Science, 337, 1078-1081, doi: 10.1126/science.1223447, 2012.
716 Chan, T. W., Brook, J. R., Smallwood, G. J., and Lu, G.: Time-resolved measurements
717 of black carbon light absorption enhancement in urban and near-urban locations of
718 southern Ontario, Canada, Atmos. Chem. Phys., 11, 10407-10432, doi:
719 10.5194/acp-11-10407-2011, 2011.
720 Chand, D., Wood, R., Anderson, T. L., Satheesh, S. K., and Charlson, R. J.:
721 Satellite-derived direct radiative effect of aerosols dependent on cloud cover, Nat.
722 Geosci., 2, 181-184, doi: 10.1038/ngeo437, 2009.
723 China, S., Mazzoleni, C., Gorkowski, K., Aiken, A. C., and Dubey, M. K.:
724 Morphology and mixing state of individual freshly emitted wildfire carbonaceous
725 particles, Nat. Commun., 4, 2122, doi: 10.1038/ncomms3122, 2013.
726 DeCarlo, P. F., Slowik, J. G., Worsnop, D. R., Davidovits, P., and Jimenez, J. L.:
727 Particle morphology and density characterization by combined mobility and
728 aerodynamic diameter measurements. Part 1: theory, Aerosol Sci. Technol., 38,
729 1185-1205, doi: 10.1080/027868290903907, 2004.
730 Giordano, M., Espinoza, C., and Asa-Awuku, A.: Experimentally measured
731 morphology of biomass burning aerosol and its impacts on CCN ability, Atmos.
732 Chem. Phys., 15, 1807-1821, doi: 10.5194/acp-15-1807-2015, 2015.
733 Hand, J. L., Day, D. E., McMeeking, G. M., Levin, E. J. T., Carrico, C. M.,
734 Kreidenweis, S. M., Malm, W. C., Laskin, A., and Desyaterik, Y.: Measured and
735 modeled humidification factors of fresh smoke particles from biomass burning: role
736 of inorganic constituents, Atmos. Chem. Phys., 10, 6179-6194, doi:
737 10.5194/acp-10-6179-2010, 2010.
738 Healy, R. M., Evans, G. J., Murphy, M., Sierau, B., Arndt, J., McGillicuddy, E.,
739 O'Connor, I. P., Sodeau, J. R., and Wenger, J. C.: Single-particle speciation of
740 alkylamines in ambient aerosol at five European sites, Anal. Bioanal. Chem., 407,
741 5899-5909, doi: 10.1007/s00216-014-8092-1, 2015.
742 Hinds, W. C.: Aerosol Technology: Properties, behavior, and measurement of airborne
743 particles, Wiley, 1999.
744 Hoffer, A., Gelencsér, A., Guyon, P., Kiss, G., Schmid, O., Frank, G. P., Artaxo, P.,
745 and Andreae, M. O.: Optical properties of humic-like substances (HULIS) in
746 biomass-burning aerosols, Atmos. Chem. Phys., 6, 3563-3570, doi:

747 10.5194/acp-6-3563-2006, 2006.
748 Hopkins, R. J., Lewis, K., Desyaterik, Y., Wang, Z., Tivanski, A. V., Arnott, W. P.,
749 Laskin, A., and Gilles, M. K.: Correlations between optical, chemical and physical
750 properties of biomass burn aerosols, Geophys. Res. Lett., 34, doi:
751 10.1029/2007gl030502, 2007.
752 Hu, M., Peng, J., Sun, K., Yue, D., Guo, S., Wiedensohler, A., and Wu, Z.: Estimation
753 of size-resolved ambient particle density based on the measurement of aerosol
754 number, mass, and chemical size distributions in the winter in Beijing, Environ. Sci.
755 Technol., 46, 9941-9947, doi: 10.1021/es204073t, 2012.
756 Huang, Y., Li, L., Li, J., Wang, X., Chen, H., Chen, J., Yang, X., Gross, D., Wang, H.,
757 and Qiao, L.: A case study of the highly time-resolved evolution of aerosol
758 chemical and optical properties in urban Shanghai, China, Atmos. Chem. Phys., 13,
759 3931-3944, doi: 10.5194/acp-13-3931-2013, 2013.
760 Huo, J., Lu, X., Wang, X., Chen, H., Ye, X., Gao, S., Gross, D. S., Chen, J., and Yang,
761 X.: Online single particle analysis of chemical composition and mixing state of
762 crop straw burning particles: from laboratory study to field measurement, Front.
763 Env. Sci. Eng., 10, 244-252, doi: 10.1007/s11783-015-0768-z, 2016.
764 Jacobson, M. Z.: Isolating nitrated and aromatic aerosols and nitrated aromatic gases
765 as sources of ultraviolet light absorption, J. Geophys. Res.-Atmos., 104, 3527-3542,
766 doi: 10.1029/1998jd100054, 1999.
767 Jacobson, M. Z.: Strong radiative heating due to the mixing state of black carbon in
768 atmospheric aerosols, Nature, 409, 695-697, doi: 10.1038/35055518, 2001.
769 Johnson, G., Ristovski, Z., and Morawska, L.: Application of the VH-TDMA
770 technique to coastal ambient aerosols, Geophys. Res. Lett., 31,
771 doi:10.1029/2004gl020126, 2004a.
772 Johnson, G. R., Ristovski, Z., and Morawska, L.: Method for measuring the
773 hygroscopic behaviour of lower volatility fractions in an internally mixed aerosol, J.
774 Aerosol Sci., 35, 443-455, doi:10.1016/j.jaerosci.2003.10.008, 2004b.
775 Katrib, Y., Martin, S. T., Rudich, Y., Davidovits, P., Jayne, J. T., and Worsnop, D. R.:
776 Density changes of aerosol particles as a result of chemical reaction, Atmos. Chem.
777 Phys., 5, 275-291, doi: 10.5194/acp-5-275-2005, 2005.
778 Kelly, W. P., and McMurry, P. H.: Measurement of particle density by inertial
779 classification of differential mobility analyzer–generated monodisperse aerosols,
780 Aerosol Sci. Technol., 17, 199-212, doi: 10.1080/02786829208959571, 1992.
781 Knudsen, J. N., Jensen, P. A., and Dam-Johansen, K.: Transformation and release to
782 the gas phase of Cl, K, and S during combustion of annual biomass, Energ. Fuel.,
783 18, 1385-1399, doi: 10.1021/ef049944q, 2004.
784 Lack, D. A., and Cappa, C. D.: Impact of brown and clear carbon on light absorption
785 enhancement, single scatter albedo and absorption wavelength dependence of black
786 carbon, Atmos. Chem. Phys., 10, 4207-4220, doi: 10.5194/acp-10-4207-2010,
787 2010.
788 Lack, D. A., Langridge, J. M., Bahreini, R., Cappa, C. D., Middlebrook, A. M., and
789 Schwarz, J. P.: Brown carbon and internal mixing in biomass burning particles, P.
790 Natl. Acad. Sci. USA, 109, 14802-14807, doi: 10.1073/pnas.1206575109, 2012.

Laskin, A., Laskin, J., and Nizkorodov, S. A.: Chemistry of atmospheric brown carbon, Chem. Rev., 115, 4335-4382, doi: 10.1021/cr5006167, 2015.

Lee, A. K. Y., Willis, M. D., Healy, R. M., Wang, J. M., Jeong, C.-H., Wenger, J. C., Evans, G. J., and Abbatt, J. P. D.: Single-particle characterization of biomass burning organic aerosol (BBOA): evidence for non-uniform mixing of high molecular weight organics and potassium, Atmos. Chem. Phys., 16, 5561-5572, doi: 10.5194/acp-16-5561-2016, 2016.

Leskinen, A. P., Jokiniemi, J. K., and Lehtinen, K. E. J.: Characterization of aging wood chip combustion aerosol in an environmental chamber, Atmos. Environ., 41, 3713-3721, doi: 10.1016/j.atmosenv.2006.12.016, 2007.

Li, C., Ma, Z., Chen, J., Wang, X., Ye, X., Wang, L., Yang, X., Kan, H., Donaldson, D. J., and Mellouki, A.: Evolution of biomass burning smoke particles in the dark, Atmos. Environ., 120, 244-252, doi: 10.1016/j.atmosenv.2015.09.003, 2015.

Li, C., Hu, Y., Chen, J., Ma, Z., Ye, X., Yang, X., Wang, L., Wang, X., and Mellouki, A.: Physiochemical properties of carbonaceous aerosol from agricultural residue burning: Density, volatility, and hygroscopicity, Atmos. Environ., 140, 94-105, doi:10.1016/j.atmosenv.2016.05.052, 2016.

Li, L., Huang, Z., Dong, J., Li, M., Gao, W., Nian, H., Fu, Z., Zhang, G., Bi, X., Cheng, P., and Zhou, Z.: Real time bipolar time-of-flight mass spectrometer for analyzing single aerosol particles, Int. J. Mass Spectrom., 303, 118-124, doi: 10.1016/j.ijms.2011.01.017, 2011.

Lide, D. R.: CRC handbook of chemistry and physics, CRC, Taylor and Francis, 2008.

Liu, S., Aiken, A. C., Gorkowski, K., Dubey, M. K., Cappa, C. D., Williams, L. R., Herndon, S. C., Massoli, P., Fortner, E. C., Chhabra, P. S., Brooks, W. A., Onasch, T. B., Jayne, J. T., Worsnop, D. R., China, S., Sharma, N., Mazzoleni, C., Xu, L., Ng, N. L., Liu, D., Allan, J. D., Lee, J. D., Fleming, Z. L., Mohr, C., Zotter, P., Szidat, S., and Prevot, A. S.: Enhanced light absorption by mixed source black and brown carbon particles in UK winter, Nat. Commun., 6, 8435, doi: 10.1038/ncomms9435, 2015.

Martins, J. V., Hobbs, P. V., Weiss, R. E., and Artaxo, P.: Sphericity and morphology of smoke particles from biomass burning in Brazil, J. Geophys. Res.-Atmos., 103, 32051-32057, doi: 10.1029/98jd01153, 1998.

Martinsson, J., Eriksson, A. C., Nielsen, I. E., Malmborg, V. B., Ahlberg, E., Andersen, C., Lindgren, R., Nystrom, R., Nordin, E. Z., Brune, W. H., Svenningsson, B., Swietlicki, E., Boman, C., and Pagels, J. H.: Impacts of combustion conditions and photochemical processing on the light absorption of biomass combustion aerosol, Environ. Sci. Technol., 49, 14663-14671, doi: 10.1021/acs.est.5b03205, 2015.

McMeeking, G. R., Fortner, E., Onasch, T. B., Taylor, J. W., Flynn, M., Coe, H., and Kreidenweis, S. M.: Impacts of nonrefractory material on light absorption by aerosols emitted from biomass burning, J. Geophys. Res.-Atmos., 119, 2014JD021750, doi: 10.1002/2014JD021750, 2014.

McMurry, P. H., Wang, X., Park, K., and Ehara, K.: The relationship between mass and mobility for atmospheric particles: a new technique for measuring particle

density, Aerosol Sci. Technol., 36, 227-238, doi: 10.1080/027868202753504083, 2002.
Moffet, R. C., Qin, X. Y., Rebotier, T., Furutani, H., and Prather, K. A.: Chemically segregated optical and microphysical properties of ambient aerosols measured in a single-particle mass spectrometer, J. Geophys. Res.-Atmos., 113, doi: 10.1029/2007jd009393, 2008.
Moffet, R. C., and Prather, K. A.: In-situ measurements of the mixing state and optical properties of soot with implications for radiative forcing estimates, P. Natl. Acad. Sci. USA, 106, 11872-11877, doi: 10.1073/pnas.0900040106, 2009.
Naeher, L. P., Brauer, M., Lipsett, M., Zelikoff, J. T., Simpson, C. D., Koenig, J. Q., and Smith, K. R.: Woodsmoke health effects: a review, Inhal. toxicol., 19, 67-106, doi: 10.1080/08958370600985875, 2007.
Nakayama, T., Ikeda, Y., Sawada, Y., Setoguchi, Y., Ogawa, S., Kawana, K., Mochida, M., Ikemori, F., Matsumoto, K., and Matsumi, Y.: Properties of light-absorbing aerosols in the Nagoya urban area, Japan, in August 2011 and January 2012: Contributions of brown carbon and lensing effect, J. Geophys. Res.-Atmos., 119, 12721-12739, doi: 10.1002/2014jd021744, 2014.
Onasch, T. B., Massoli, P., Kebabian, P. L., Hills, F. B., Bacon, F. W., and Freedman, A.: Single scattering albedo monitor for airborne particulates, Aerosol Sci. Technol., 49, 267-279, doi: 10.1080/02786826.2015.1022248, 2015.
Park, R., Jacob, D., Kumar, N., and Yantosca, R.: Regional visibility statistics in the United States: Natural and transboundary pollution influences, and implications for the Regional Haze Rule, Atmos. Environ., 40, 5405-5423, doi: 10.1016/j.atmosenv.2006.04.059, 2006.
Petters, M. D., Carrico, C. M., Kreidenweis, S. M., Prenni, A. J., DeMott, P. J., Collett, J. L., and Moosmuller, H.: Cloud condensation nucleation activity of biomass burning aerosol, J. Geophys. Res.-Atmos., 114, 16, doi: 10.1029/2009jd012353, 2009.
Philippin, S., Wiedensohler, A., and Stratmann, F.: Measurements of non-volatile fractions of pollution aerosols with an eight-tube volatility tandem differential mobility analyzer (VTDMA-8), J. Aerosol Sci., 35, 185-203, doi: 10.1016/j.jaerosci.2003.07.004, 2004.
Pitz, M., Schmid, O., Heinrich, J., Birmili, W., Maguhn, J., Zimmermann, R., Wichmann, H. E., Peters, A., and Cyrys, J.: Seasonal and diurnal variation of PM2.5 apparent particle density in urban air in Augsburg, Germany, Environ. Sci. Technol., 42, 5087-5093, doi: 10.1021/es7028735, 2008.
Rissler, J., Nordin, E. Z., Eriksson, A. C., Nilsson, P. T., Frosch, M., Sporre, M. K., Wierzbicka, A., Svenningsson, B., Londahl, J., Messing, M. E., Sjogren, S., Hemmingsen, J. G., Loft, S., Pagels, J. H., and Swietlicki, E.: Effective density and mixing state of aerosol particles in a near-traffic urban environment, Environ. Sci. Technol., 48, 6300-6308, doi: 10.1021/es5000353, 2014.
Saleh, R., Robinson, E. S., Tkacik, D. S., Ahern, A. T., Liu, S., Aiken, A. C., Sullivan, R. C., Presto, A. A., Dubey, M. K., Yokelson, R. J., Donahue, N. M., and Robinson, A. L.: Brownness of organics in aerosols from biomass burning linked to their

879 black carbon content, Nat. Geosci., 7, 647-650, doi: 10.1038/ngeo2220, 2014.
880 Schmid, O., Karg, E., Hagen, D. E., Whitefield, P. D., and Ferron, G. A.: On the
881 effective density of non-spherical particles as derived from combined
882 measurements of aerodynamic and mobility equivalent size, J. Aerosol Sci., 38,
883 431-443, doi: 10.1016/j.jaerosci.2007.01.002, 2007.
884 Schnaiter, M., Linke, C., Mohler, O., Naumann, K. H., Saathoff, H., Wagner, R.,
885 Schurath, U., and Wehner, B.: Absorption amplification of black carbon internally
886 mixed with secondary organic aerosol, J. Geophys. Res.-Atmos., 110, doi:
887 10.1029/2005jd006046, 2005.
888 Schwarz, J., Spackman, J., Fahey, D., Gao, R., Lohmann, U., Stier, P., Watts, L.,
889 Thomson, D., Lack, D., and Pfister, L.: Coatings and their enhancement of black
890 carbon light absorption in the tropical atmosphere, J. Geophys. Res.-Atmos., 113,
891 doi: 10.1029/2007JD009042, 2008.
892 Silva, P. J., Liu, D. Y., Noble, C. A., and Prather, K. A.: Size and chemical
893 characterization of individual particles resulting from biomass burning of local
894 Southern California species, Environ. Sci. Technol., 33, 3068-3076, doi:
895 10.1021/es980544p, 1999.
896 Song, X. H., Hopke, P. K., Fergenson, D. P., and Prather, K. A.: Classification of
897 single particles analyzed by ATOFMS using an artificial neural network, ART-2A,
898 Anal. Chem., 71, 860-865, doi: 10.1021/ac9809682, 1999.
899 Spackman, J. R., Gao, R. S., Neff, W. D., Schwarz, J. P., Watts, L. A., Fahey, D. W.,
900 Holloway, J. S., Ryerson, T. B., Peischl, J., and Brock, C. A.: Aircraft observations
901 of enhancement and depletion of black carbon mass in the springtime Arctic, Atmos.
902 Chem. Phys., 10, 9667-9680, doi: 10.5194/acp-10-9667-2010, 2010.
903 Spencer, M. T., Shields, L. G., and Prather, K. A.: Simultaneous measurement of the
904 effective density and chemical composition of ambient aerosol particles, Environ.
905 Sci. Technol., 41, 1303-1309, doi: 10.1021/es061425+, 2007.
906 Tajima, N., Fukushima, N., Ehara, K., and Sakurai, H.: Mass range and optimized
907 operation of the aerosol particle mass analyzer, Aerosol Sci. Technol., 45, 196-214,
908 doi: 10.1080/02786826.2010.530625, 2011.
909 Turpin, B. J., and Lim, H.-J.: Species contributions to PM2.5 mass concentrations:
910 revisiting common assumptions for estimating organic mass, Aerosol Sci. Technol.,
911 35, 602-610, doi: 10.1080/02786820119445, 2001.
912 Wentzel, M., Gorzawski, H., Naumann, K. H., Saathoff, H., and Weinbruch, S.:
913 Transmission electron microscopical and aerosol dynamical characterization of soot
914 aerosols, J. Aerosol Sci., 34, 1347-1370, doi: 10.1016/s0021-8502(03)00360-4,
915 2003.
916 You, R., Radney, J. G., Zachariah, M. R., and Zangmeister, C. D.: Measured
917 Wavelength-Dependent Absorption Enhancement of Internally Mixed Black
918 Carbon with Absorbing and Nonabsorbing Materials, Environ. Sci. Technol., doi:
919 10.1021/acs.est.6b01473, 2016.
920 Zauscher, M. D., Wang, Y., Moore, M. J. K., Gaston, C. J., and Prather, K. A.: Air
921 Quality Impact and Physicochemical Aging of Biomass Burning Aerosols during
922 the 2007 San Diego Wildfires, Environ. Sci. Technol., 47, 7633-7643, doi:

10.1021/es4004137, 2013.
Zhai, J., Wang, X., Li, J., Xu, T., Chen, H., Yang, X., and Chen, J.: Thermal desorption single particle mass spectrometry of ambient aerosol in Shanghai, Atmos. Environ., 123, 407-414, doi: 10.1016/j.atmosenv.2015.09.001, 2015.
Zhang, R., Khalizov, A. F., Pagels, J., Zhang, D., Xue, H., and McMurry, P. H.: Variability in morphology, hygroscopicity, and optical properties of soot aerosols during atmospheric processing, P. Natl. Acad. Sci. USA, 105, 10291-10296, doi: 10.1073/pnas.0804860105, 2008.
Zhang, Y., Zhang, Q., Cheng, Y., Su, H., Kecorius, S., Wang, Z., Wu, Z., Hu, M., Zhu, T., Wiedensohler, A., and He, K.: Measuring the morphology and density of internally mixed black carbon with SP2 and VTDMA: new insight into the absorption enhancement of black carbon in the atmosphere, Atmos. Meas. Tech., 9, 1833-1843, doi: 10.5194/amt-9-1833-2016, 2016

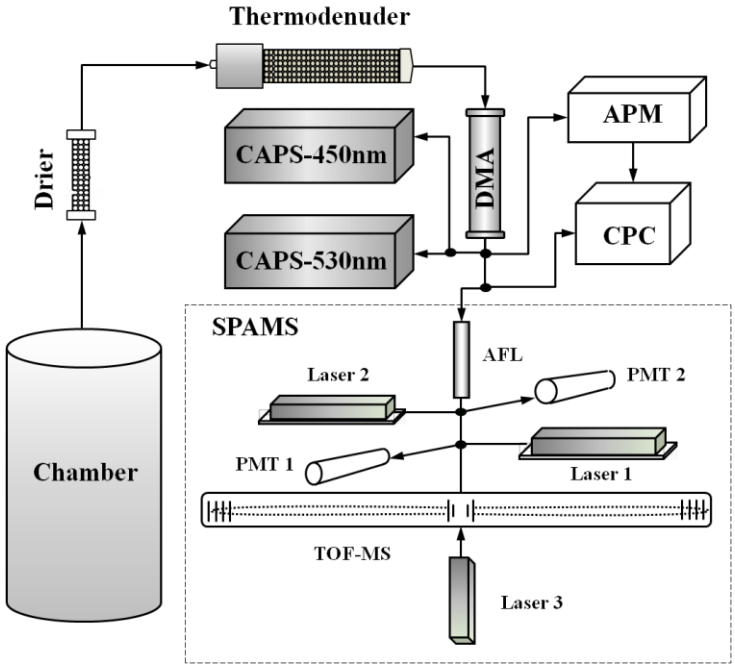

Figure 1. Schematic of the instrumental setup. The CAPS, DMA, CPC, APM and SPAMS represent Cavity Attenuated Phase Shift spectroscopy, Differential Mobility Analyzer, Condensation Particle Counter, Aerosol Particle Mass analyzer and Single Particle Aerosol Mass Spectrometer, respectively.

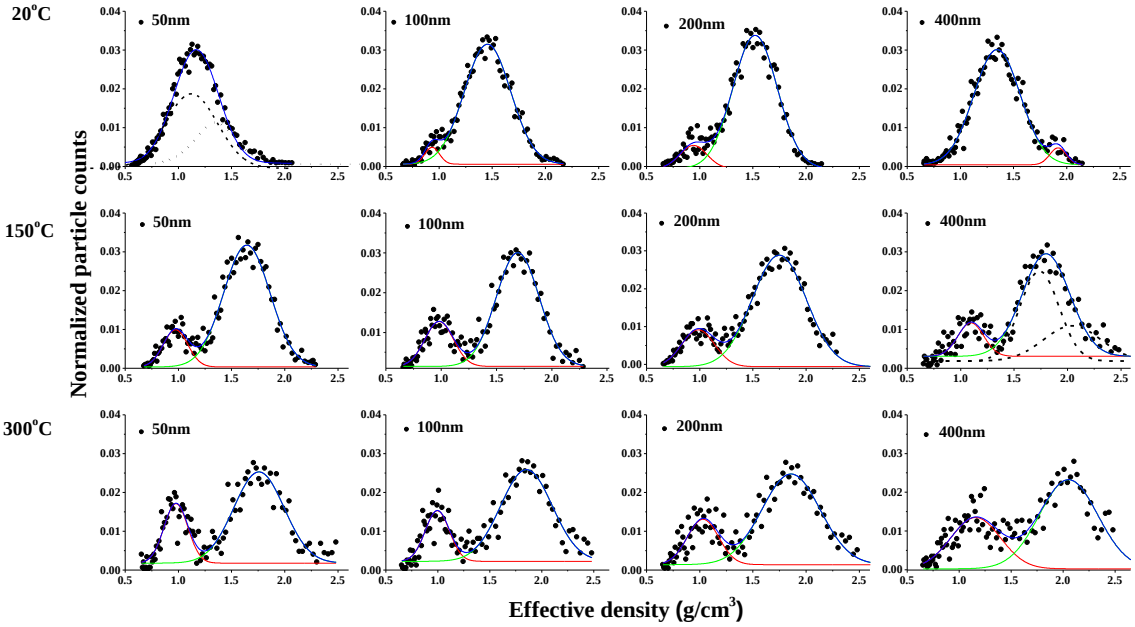

Figure 2. Average density distributions of 50, 100, 200, and 400 nm particles selected by DMA at 20 °C (room temperature), 150 °C, and 300 °C. Gaussian model was applied in fitting each density scan (red and green lines). Black dashes were the assumption Gaussian models application.

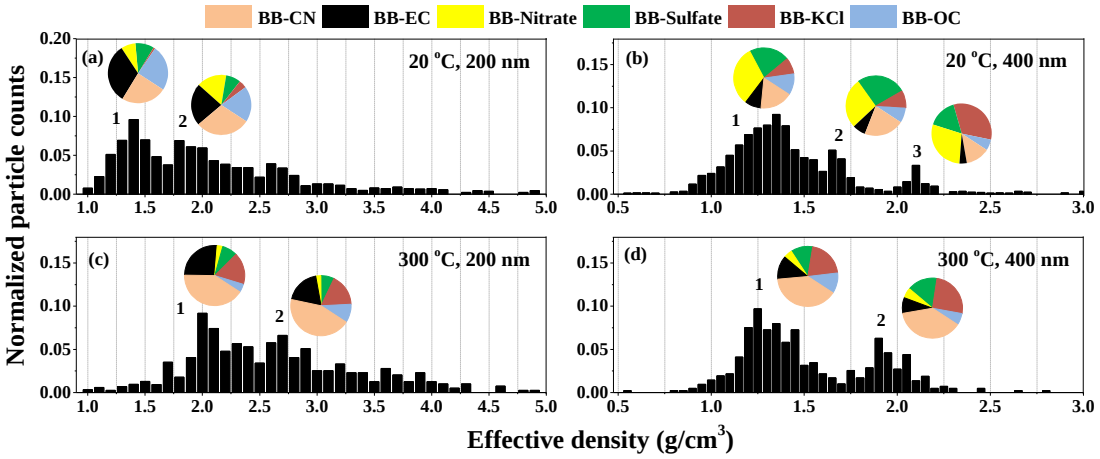

Figure 3. Vacuum aerodynamic size distributions detected by the SPAMS of 200 nm and 400 nm electrical mobility size-selected biomass burning particles and pie charts for the particle types in different aerodynamic modes at 20 °C (room temperature) and 300 °C.

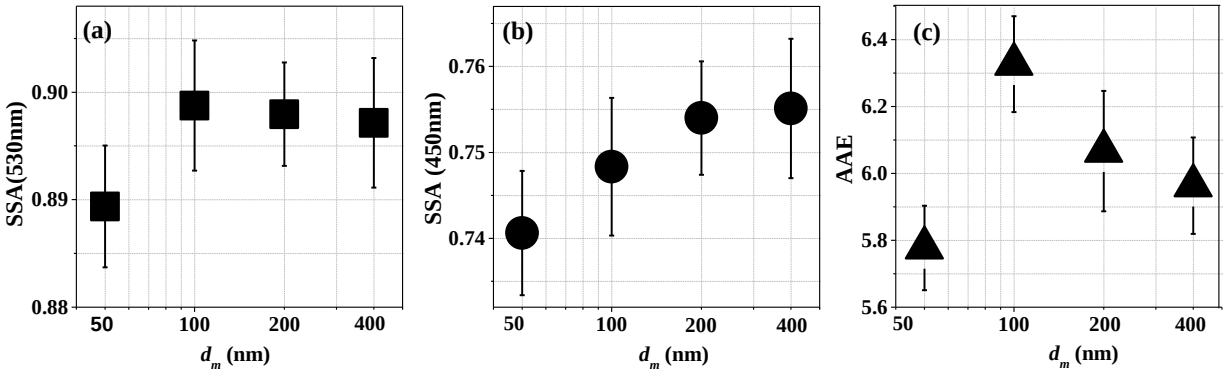

Figure 4. (a)-(b): Size-resolved single scattering albedo (SSA) at wavelengths of 530 nm and 450 nm. (c): Ångström absorption exponent (AAE) of biomass burning particles at room temperature (20^{o}C).

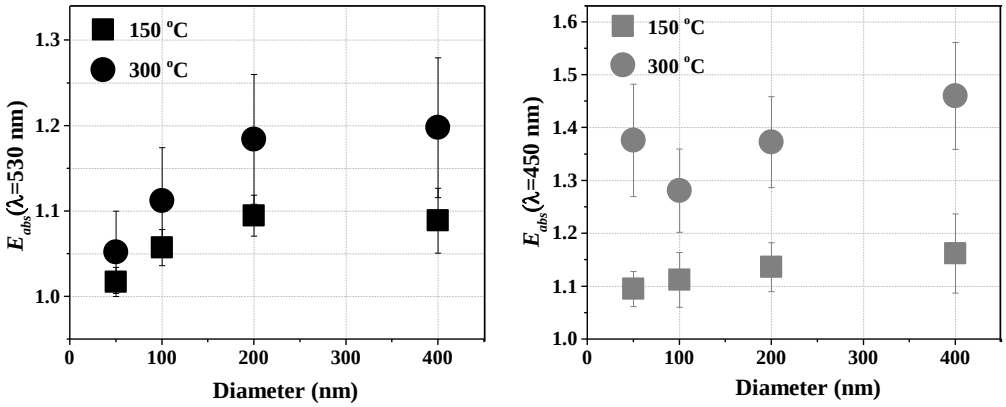

Figure 5. The size-resolved absorption enhancement (E_{abs}) at wavelengths of 450 nm and 530 nm.